Case Studies in Thermal Engineering 78 (2026) 107668

Contents lists available at ScienceDirect

Case Studies in Thermal Engineering

journal homepage: www.elsevier.com/locate/csite

Design optimization of a circular enclosure with flexible fins: Fluid-Structure interaction and heat transfer analysis using rotating frame modeling

Ali Qassim Abd Al-Hassan [a], Muneer A. Ismael [a,b], Mohammad Ghalambaz [c,d], Ali Chamkha [e], Mohamed Bechir Ben Hamida [f,*]

[a] Mechanical Engineering Department, College of Engineering, University of Basrah, Basrah, Iraq
[b] College of Engineering, University of Warith Al-Anbiyaa, Karbala, Iraq
[c] Department of Mathematical Sciences, Saveetha School of Engineering, SIMATS, Chennai, India
[d] Refrigeration and Air Conditioning Technical Engineering Department, College of Technical Engineering, The Islamic University, Najaf, Iraq
[e] Faculty of Engineering, Kuwait College of Science and Technology, Doha District, 35004, Kuwait
[f] Deanship of Scientific Research, Imam Mohammad Ibn Saud Islamic University (IMSIU), Riyadh, Saudi Arabia

GRAPHICAL ABSTRACT

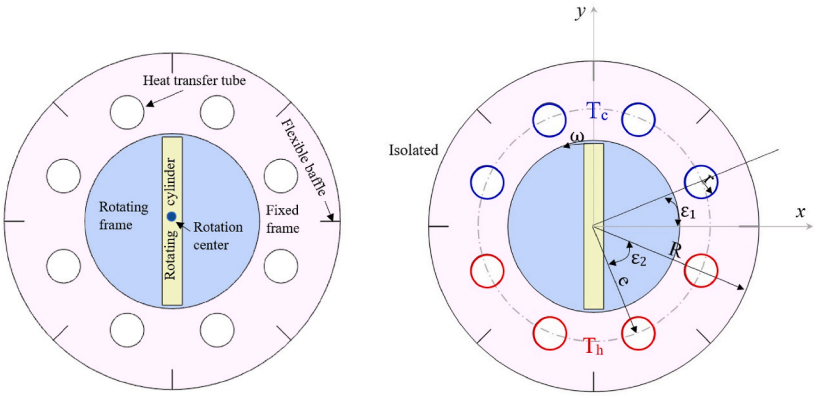

* Corresponding author.
E-mail addresses: aliqassim1986@gmail.com (A.Q. Abd Al-Hassan), MBHamida@imamu.edu.sa (M.B. Ben Hamida).

https://doi.org/10.1016/j.csite.2026.107668
Received 25 June 2025; Received in revised form 19 November 2025; Accepted 7 January 2026
Available online 7 January 2026

ARTICLE INFO

Keywords:
Optimization
Enhanced heat transfer
Rotating frame
Cylinders
Rotational mesh
Fluid-structure interaction (FSI)

ABSTRACT

This study optimizes heat transfer in a circular vessel containing cold and hot cylinders, a rotating frame, and flexible baffles designed to enhance thermal exchange. Optimized design of such topics improves the performance of heat exchangers. The investigation analyzes the impact of rotational speeds ($\omega^* = 10$–400), distances of the cylinders from the frame axis ($e^* = 0.32$–0.43), and Rayleigh number ($Ra = 10^3$–10^5) on the heat transfer. Time-dependent equations are discretized and solved using the finite element method with rotating meshes. The Nelder-Mead optimization method was utilized to identify the optimal conditions that enhance the system's thermal stability and heat exchange efficiency. This approach establishes a foundation for improved thermal designs for applications requiring high dynamic thermal responsiveness. The results indicated that the maximum heat exchanges were obtained at $e^* = 0.32378$ and $\omega^* = 366.48$ for $Ra = 10^3$, and at $e^* = 0.32$ and $\omega^* = 379.43$ for $Ra = 10^5$. The Nusselt numbers for these conditions were 5.32 and 7.7, respectively. Therefore, to achieve optimal heat transfer, the operating conditions, such as the frame's angular speed and the cylinder's distance, should be optimized for each Rayleigh number.

Nomenclature

a	Length, m	T	Temperature, K
A	Oscillation amplitude, m	u, v	Velocity of fluid, m s^{-1}
b	Width, m	$\vec{V}$	Velocity vector (absolute), m s^{-1}
C_p	Specific heat, J kg^{-1} K^{-1}	$\vec{W}$	Velocity vector (relative), m s^{-1}
$d_{fl.}$	Displacement, m	$\vec{W}_{co.}$	Component of velocity vector, m s^{-1}
D	Vessel diameter (2R), m	$\vec{W}_{fl.}$	The velocity vector of the moving coordinate, m s^{-1}
Di	Agitator diameter, m	**Greek**	
e	Distance between the cylinder to the vessel center, m	α	Diffusivity of thermal, m^2 s^{-1}
E	Elastic modulus, N m^{-2}	β	Fluid's thermal expansion coefficient, K^{-1}
$\vec{F}_b$	Vector of body force, N m^{-3}	θ	Non-dimensional temperature
k	Thermal conductivity, Wm^{-1} K^{-1}	μ	Dynamic viscosity, kg m^{-1} s^{-1}
k_f	Fluid thermal conductivity, Wm^{-1} K^{-1}	ρ	Density, kg m^{-3}
k_r	The conductivity ratio between the solid (flexible baffle) and fluid	υ	Fluid's kinematic viscosity, m^2 s^{-1}
k_s	the solid's conductivity, Wm^{-1} K^{-1}	$\omega, \vec{\omega}$	Frame's angular velocity, vector, rad s^{-1}
n	Unity normal vector	ε	The angle of the cylinder position
Nu	Nusselt number	**Subscripts**	
p	pressure, N m^{-2}	c	Cold
Pr	Prandtl number	f	Fluid
r	Cylinders radius, m	$fl.$	Flexible baffle
R	Vessel's radius, m	h	Hot
Ra	Rayleigh number	j	Vector unit aligned with the y-axis
Re	Reynolds number, $Re = \omega i\ Di^2\rho/\mu$	s	Solid
R_h	Ratio of heat capacity	0	reference value
$R_{th.}$	Ratio of thermal conductivity	**Supersubscripts**	
t	Time, s	*	Dimensionless
t_p	Oscillation period, s		

1. Introduction

Heat exchange is a vital aspect of various engineering applications, including mechanical, chemical, and aerospace engineering. The design of thermal structures plays a crucial role in enhancing performance efficiency in complex systems [1]. Effective heat exchange mechanisms are essential for maintaining optimal operating temperatures, reducing energy consumption, and increasing overall system reliability [2]. To ensure optimum heat transfer, optimization is a key strategy to attain the best heat transfer. Over the past decade, researchers have pushed topology optimization toward new boundaries, especially within metamaterial design, as surveyed by Deaton and Grandhi [3]. Traditionally, topology optimization in fluid flow has focused on determining optimal flow channels through models governed solely by fluid equations, as initially discovered by Steven et al. [4] and later studies [5–8]. Previous studies have explored the integration of heat transfer and natural convection with fluid flow equations under both steady-state and transient conditions. [9–11]. In the FSI field, however, few researchers have developed methodologies for structural topology optimization. Notably, Picelli et al. [12] significantly contributed by introducing an advanced bidirectional evolutionary structural optimization (BESO) method tailored for optimizing structures under FSI conditions. The results demonstrate the effectiveness of evolutionary methods in handling multiphysics challenges, achieving compliance minimization while adapting to fluid-induced loads throughout the optimization process.

Moreover, Bangian-Tabrizi and Jaluria [13] proposed a novel strategy for estimating unknowns in thermal systems by reducing the error between calculated and measured temperatures. This framework has demonstrated high accuracy and robustness across different types of convection, proving advantageous for applications in thermal and industrial studies. Subramaniam et al. [14] introduced a

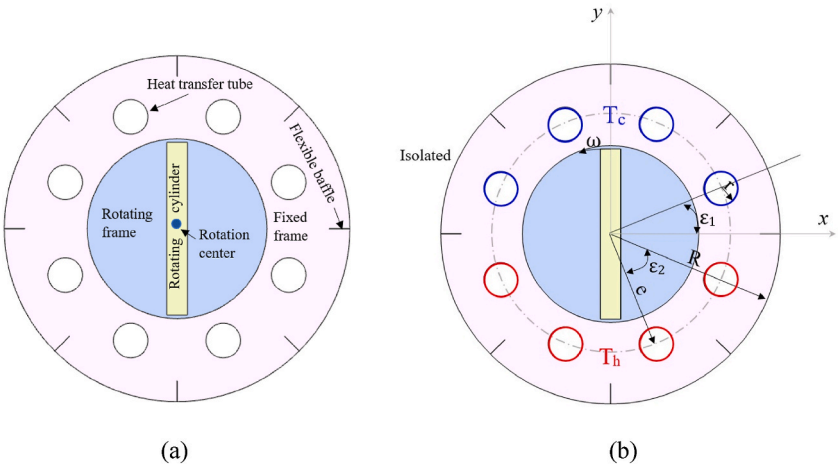

Fig. 1. Schematic and coordinate system of the problem (a) the domain regions and (b) the geometrical details.

topology optimization method that maximizes heat transfer from multiple sources while minimizing pressure drop, allowing for the design of integrated heat transfer systems with enhanced thermal management and low fluid resistance. Similarly, Kwon et al. [15] utilized 3D-printed static mixers to improve heat transfer in laminar flows, identifying optimized arrays that offer superior mixing and thermal performance while minimizing pressure drop in thermochemical heat storage. Chen et al. [16] and Dehghani et al. [17] applied topology optimization focused on material layout to maximize thermal conductivity and energy storage density throughout the system. These optimized layouts enable more efficient energy distribution, making them valuable for sustainable energy storage. Likewise, Li et al. [18] employed fluid-structure interaction (FSI) analysis on serrated baffle shapes in plate-fin heat exchangers, proposing configurations that improve thermal enhancement with minimal impact on pressure. Computational fluid dynamics (CFD) is widely applied in optimizing operational parameters for real engineering problems [19–21]. Topologically optimized designs have recently been explored for complex physical challenges, such as fluid dynamics [22] and electromagnetics [23]. The inherent nonlinearity in equations like the Navier–Stokes equations in fluid dynamics and many state variables pose significant challenges, as does solving Maxwell's equations in electromagnetics. Rees et al. [24] employed a proprietary topology optimization algorithm to evaluate a crossflow two-fluid heat exchanger based on a periodic unit cell. Gangadhar et al. [25] investigated hybrid nanofluids, examining alumina–copper/water hybrid nanofluids and analyzing the effects of thermal radiation and Lorentz forces on velocity and temperature distributions. Their findings suggest hybrid nanoparticles offer superior thermal performance to mono-nanofluids, highlighting their potential in engineering-related thermal management applications.

The study presented by Al-Hasan et al. [26] reveals the importance of a circular enclosure containing cold and hot cylinders and a rotating mixer in heat transfer applications in industrial facilities, where the rotation of the internal cylinder [27–30], or plates [31,32] helps in promoting the mixed heat transfer more efficiently. Moreover, the heat transfer process becomes more advanced with the incorporation of flexible baffles [33–35]. Al-Hasan et al. [36] have found that using flexible fins within a circular enclosure containing a rotating bar improves not only the heat transfer, but also reduces the skin friction by mitigating the effect of vortices generated by the rotation. Ikram et al. [37–39] explored heat transfer and flow characteristics in hexagonal cavities with dynamic modulators, emphasizing the influence of modulator movement and geometric design on thermal efficiency and performance. Jalili et al. [40–42], Roshani et al. [43], Bahnami et al. [44], and Zhang et al. [45] investigated heat and mass transfer, natural and forced convection, and MHD effects in various porous and non-porous cavities of different shapes, analyzing the influence of barriers, vanes, magnetic fields, buoyancy, and cavity geometry on Nusselt number, flow behavior, and thermal performance.

Therefore, in this study, incorporating a series of flexible baffles distributed on the internal perimeter of the circular enclosure [26] leads to a multitude of variables that require special control to obtain the best combination. The present study addresses complex interdependencies between fluid flow, structural deformation, and heat exchange, offering unprecedented efficiencies and performance enhancements in critical industrial sectors. The FSI problem itself is inherently complex, involving the coupled behavior of fluid flow and heat exchange. When applied to a vessel involving rotating frame, this complexity is further amplified by the complicated flow behaviors, which significantly influence both fluid dynamics and structural integrity. Therefore, the introduction of an optimization algorithm allows for the systematic exploration of design parameters, leading to configurations that maximize heat transfer efficiency. The rotational speed of the mixer $10 \leq \omega^* \leq 400$, the distribution the hot and cold inner cylinders $0.32 \leq e^* \leq 0.43$, and the Rayleigh number $10^3 \leq \mathrm{Ra} \leq 10^5$ are the targeted parameters to determine the optimal conditions for maximizing heat transfer within the system. Results of this study are significant in the chemical industry, as they improve the efficiency of reactor designs, enhance heat recovery systems, and optimize process control, ultimately reducing operational costs.

2. Mathematical formulation

As given in Fig. 1, this study examines a vessel with radius (R) and a central rotating conductive frame. The rotating rectangular

frame has dimensions defined by a width ($b = 0.12\,R$) and length ($a = R$). The frame's heat capacity and thermal conductivity ratio are denoted as (R_h) and (R_{th}). The frame rotates counterclockwise around its center at an angular velocity (ω). Additionally, bundles of cylinders are arranged along the vessel's periphery, adjacent to the vessel's wall.

Eight isothermal cylinders have been distributed inside the vessel, with the upper four kept at a constant cold temperature (Tc), while the lower four are maintained at a constant hot temperature (Th). The interval between these cylinders is 45°. The vessel is filled with water, characterized by a Prandtl number (Pr = 6.90). Additionally, eight flexible baffles are uniformly distributed along the vessel's periphery, each positioned between two adjacent cylinders. The baffles have lengths and widths defined by ($a_{fl} = 0.12$ R) and ($b_{fl} = 0.002$ R), respectively. A dimensionless parameter ($k_r = 13$) represents the thermal conductivity ratio, reflecting the ratio between the thermal conductivities of the flexible baffles' solid material and the surrounding fluid. A no-slip boundary condition is applied to the solid boundaries. Given the assembly's extended dimension along the z-axis, including the rotating frame, the problem is approximated as a two-dimensional (2D) geometry in the x-y plane. The density varies with temperature, governed by the Boussinesq approximation, which introduces a body force into the system. The fluid is assumed to behave as Newtonian fluids and incompressible, whereas the flow is limited to laminar regime. Except for the density, the other properties are considered constant with temperature, and the flexible fins are not affected by temperature. The governing equations, incorporating the Boussinesq's approximation, are given as [46–48].

$$\nabla.\vec{W} = 0 \tag{1}$$

$$\rho\frac{\partial\vec{V}}{\partial t} + \rho\nabla.\left(\vec{W}_{co.}\otimes\vec{V}\right) + \rho\left(\vec{\omega}\times\vec{V}\right) - \vec{F}_b - \nabla.\left(\mu\nabla\vec{V}\right) = -\nabla p \tag{2}$$

$$\rho C_p\frac{\partial T}{\partial t} + \rho C_p\nabla.\left(\vec{W}_{co.}\,T\right) - \nabla.(k\nabla T) = 0 \tag{3}$$

$$\left(\rho C_p\right)_s\frac{\partial \mathrm{T}_s}{\partial t} - \nabla.(k_s\nabla \mathrm{T}_s) = 0 \tag{4}$$

where ω is the solid frame's rotational velocity and $\vec{F}_b = \rho_0 g\beta(T - \mathrm{T}_c)j$. Here, $\vec{V} = \vec{\omega}\times\vec{r} + \vec{W}$ where $\vec{\omega}\times\vec{r}$ represents the velocity of the rotating frame, $\vec{W}$ is the relative velocity, $\vec{V}$ is the absolute velocity, and while $\left(\vec{W}_{co.} = \vec{W} - \vec{W}_{fl.}\right)$, $\vec{W}_{fl.}$ is the velocity of the moving coordinates.

The governing equations for the flexible baffle can be expressed as [33,35,36]:

$$\rho_{fl.}\frac{\partial^2 dfl.}{\partial t^2} - \nabla\sigma - \vec{\mathrm{F}}_{\mathrm{b}(fl.)} = 0 \tag{5}$$

The energy equation of the baffle [33,35,36]:

$$\frac{\partial T}{\partial t} - \alpha_{fl.}\ \nabla^2 T = 0 \tag{6}$$

where $d_{fl.}$ is the displacement vector, σ is the stress tensor, $\alpha_{fl.}$ is the thermal diffusivity of flexible baffles, and $\vec{\mathrm{F}}_{\mathrm{b}(fl.)}$ is the body force acting on the baffles $\vec{\mathrm{F}}_{\mathrm{b}(fl.)} = \rho_{fl.\ g_y}$

The elastic displacement of the baffle, caused by the forces exerted by the fluid and pressure, can be described using the Kirchhoff stress tensor, as outlined in Ref. [49].

$$\tau_{fl.} = J\,\sigma \tag{7}$$

$$\sigma = J^{-1}FZF^T \tag{8}$$

where $F = \left(1 + \nabla d_{fl.}\right), J = det(F)$, J is Jacobin determent,τ is extra stress tensor, the second Piola-Kirchhoff stress tensor, Z, is associated with the fluid strain, denoted as $\varepsilon_{\mathrm{fl.}}$ by $Z = Ci : (\varepsilon)$

Where $\varepsilon_{fl.} = \frac{1}{2}\left(\nabla \mathrm{d}_{fl.} + \nabla \mathrm{d}_{fl.}{}^T + \nabla d_{fl.}{}^T\nabla \mathrm{d}_{fl.}\right)$

Where $Ci = Ci(E, \vartheta o)$, ϑo is the Poisson ratio, Ci is the elasticity tensor, ε is the strain rate, E is the elastic modulus, and,: is the double–dot tensor product.

The following dimensionless parameters are introduced:

$$\nabla^* = \frac{\nabla}{D}, e^*, r^* = \frac{e, r}{D}\ \theta = \frac{T - T_c}{T_h - T_c}, \omega^* = \frac{\omega D^2}{\alpha_f},\ \vec{V}^* = \frac{\vec{V} D}{\alpha_f},\ \vec{W}^* = \frac{\vec{W} D}{\alpha_f}, \overrightarrow{W^*}_{co.} = \frac{\vec{W}_{co.} D}{\alpha_f}, t^* = \frac{(t\ \alpha_f)}{D^2}, Ra = \frac{g\beta D_h^3 (T_h - T_c)}{\vartheta\ \alpha_f}, p^*$$

$$= \frac{(p + \rho_0 g y)}{\left(\rho_f\ (\alpha_f / D)^2\right)}, Pr = \frac{\vartheta}{\alpha_f}, \sigma^* = \frac{\sigma}{E}, E^* = \frac{E\ D^2}{\rho_f \alpha_f{}^2} \tag{9}$$

The conservation equations have been reformulated as follows [50,51]:

$$\nabla^* . \vec{W}^* = 0 \tag{10}$$

$$\frac{\partial \vec{V}^*}{\partial t^*} + \nabla^* . \left(\overrightarrow{W^*}_{co.} \otimes \vec{V}^*\right) + \left(\vec{\omega}^* \times \vec{V}^*\right) - \vec{F}_b^* - Pr\ \nabla^{*2} \vec{V}^* = -\nabla^* p^* \tag{11}$$

$$\frac{\partial \theta}{\partial t^*} + \overrightarrow{W^*}_{co.}\ \nabla^* \theta - \nabla^{*2} \theta = 0 \tag{12}$$

$$\frac{(\rho C_p)_s}{(\rho C_p)_f} \frac{\partial \theta_s}{\partial t^*} - \left(\frac{k_s}{k_f}\right) \nabla^{*2} \theta = 0 \tag{13}$$

where $\vec{F}_b^* = jRa\ Pr\ \theta$, and the solid frame's rotational speed is represented by ω. The ratios $R_{th.}$ and R_h are recognized as:

$$R_{th.} = \frac{k_s}{k_f} \text{ and } R_h = \frac{(\rho c_p)_s}{(\rho c_p)_f} \tag{14}$$

and the equations for the flexible baffles are

$$\frac{1}{\rho_r} \frac{d^2 d_{fl.}{}^*}{dt^{*2}} - E^* \nabla \sigma^* - E^* \vec{F}^*_{b(fl.)} = 0 \tag{15}$$

$$\frac{\partial \theta}{\partial t^*} - \alpha_r \nabla^2 \theta = 0 \tag{16}$$

where $\rho_r = \frac{\rho_f}{\rho_{fl.}}$ is density ratio, and $\alpha_r = \frac{\alpha_{fl.}}{\alpha_f}$ is thermal diffusivity ratio.

Temperature boundary conditions for the vessel, expressed in dimensionless form, are as follows:

$$\theta = 0, \textit{For the four cold cylinders in the vessel's top section}, \tag{17-a}$$

$$\theta = 1, \textit{For the four hot cylinders in the lower part of the vessel} \tag{17-b}$$

$$\frac{\partial \theta}{\partial n} = 0, \textit{For the insulated outer surface of the vessel} \tag{17-c}$$

$$\theta_s = \theta_f, \textit{The boundary conditions at the outer edge of the rotating frame} \tag{17-d}$$

$$\left(\frac{\partial \theta}{\partial n}\right)_f = R_{th} \left(\frac{\partial \theta}{\partial n}\right)_s \tag{17-e}$$

$$\frac{\partial d_{fl.}{}^*}{\partial t^*} = \vec{W}^*, E^* \sigma . n = -p^* + Pr \nabla \vec{W}^*, \textit{For non} - \textit{slip boundary condition on the baffles} \tag{17-f}$$

$$\frac{\partial \theta_f}{\partial n} = k_r \frac{\partial \theta_{fl.}}{\partial n}, \textit{The interface between flexible baffles and fluid} \tag{17-g}$$

where $k_r = \frac{k_{fl.}}{k_f}$ is the ratio of thermal conductivity between flexible baffles to fluid

Impermeability and no-slip boundary conditions are imposed on all solid surfaces, ensuring velocity and shear stress continuity across stationary and rotating frames. The dominant mode of heat transfer, whether convection or conduction, is identified by evaluating the number of Nusselt along the wall of the heated cylinder [36].

$$Nu = -\frac{1}{2\pi r} \int_0^{2\pi r} \left(\frac{\partial \theta}{\partial n}\right) dS \tag{18}$$

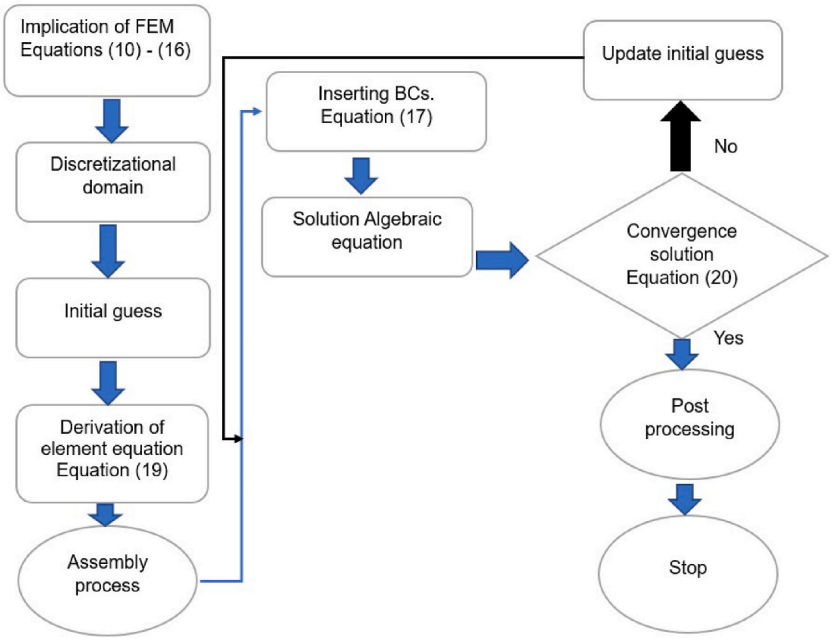

Fig. 2. Summaries the finite element method (FEM) procedure.

3. Numerical solution

The region is partitioned into distinct elements, with the finite element method (FEM) used to discretize equations (10)–(16) into discrete components. COMSOL Multiphysics (version 6) was used for the numerical solution. This software is based on the FEM, which employs nonlinear residual equations obtained by applying weighted residuals, a process commonly known as the Galerkin method. The governing equations are discretized throughout the domain, excluding regions occupied by cylinders, to ensure precise treatment of straight and curved boundaries. Basis functions compute unknown variables at each element's nodes, enabling the interpolation of temperature, pressure, and velocity fields.

$$\text{the } u^*, v^* \approx \sum_i^j (u^*, v^*)_i^{kt} \Phi_i^{kt}(x^*, y^*), \theta \approx \sum_i^j \theta_i^{kt} \Phi_i^{kt}(x^*, y^*), p^* \approx \sum_i^j p^{*kt}_i \Phi_i^{kt}(x^*, y^*) \tag{19}$$

where j shows the number of nodes, i indicate the node number, kt which means the time iteration, and Φ represents a basis function.

For the used software, the integral forms of the core equations were computed across the mesh elements, resulting in residual equations. These residuals were then tackled using a bi-level algorithm. The large, sparse linear systems were efficiently managed using the Parallel Direct Solver (PARDISO) [52–55], harnessing parallel computing to reduce computational time significantly. The equations were addressed using the method of Newton, incorporating a damping coefficient of 8×10^{-1} and adhering to a relative error threshold below (10^{-3}) for precision. To enhance stability, bi-directional upwind and transverse stabilization techniques were implemented to mitigate numerical instabilities caused by convective and diffusive effects. A time step of 0.001 was implemented. Fig. 2 illustrates the FEM methodology, detailing the numerical procedure. The computations demonstrated an error margin confined to a maximum of 5×10^{-3} across two adequate trials.

$$\left| \frac{|\Gamma^{je+1} - \Gamma^{je}|}{\Gamma^{je+1}} \right| \leq 5 \times 10^{-3} \tag{20}$$

Γ can represent the velocity, temperature, or pressure, and je denotes the iteration number.

After substituting equations, two key procedures are carried out during the numerical analysis phase. First, an appropriate mesh is generated by partitioning the domain using an automatic mesh generation algorithm. Second, the results are compared with other researchers' findings to assess the analysis's accuracy, as further elaborated in the subsequent sections.

3.1. Optimization algorithm

The Nelder–Mead method is a popular method in numerical optimization, used to solve unconstrained optimization problems involving mathematical functions that are difficult to differentiate or have properties that make calculating derivatives impractical. This method is characterized by its ability to find optimal points (maxima or minima) without needing to know or calculate derivatives,

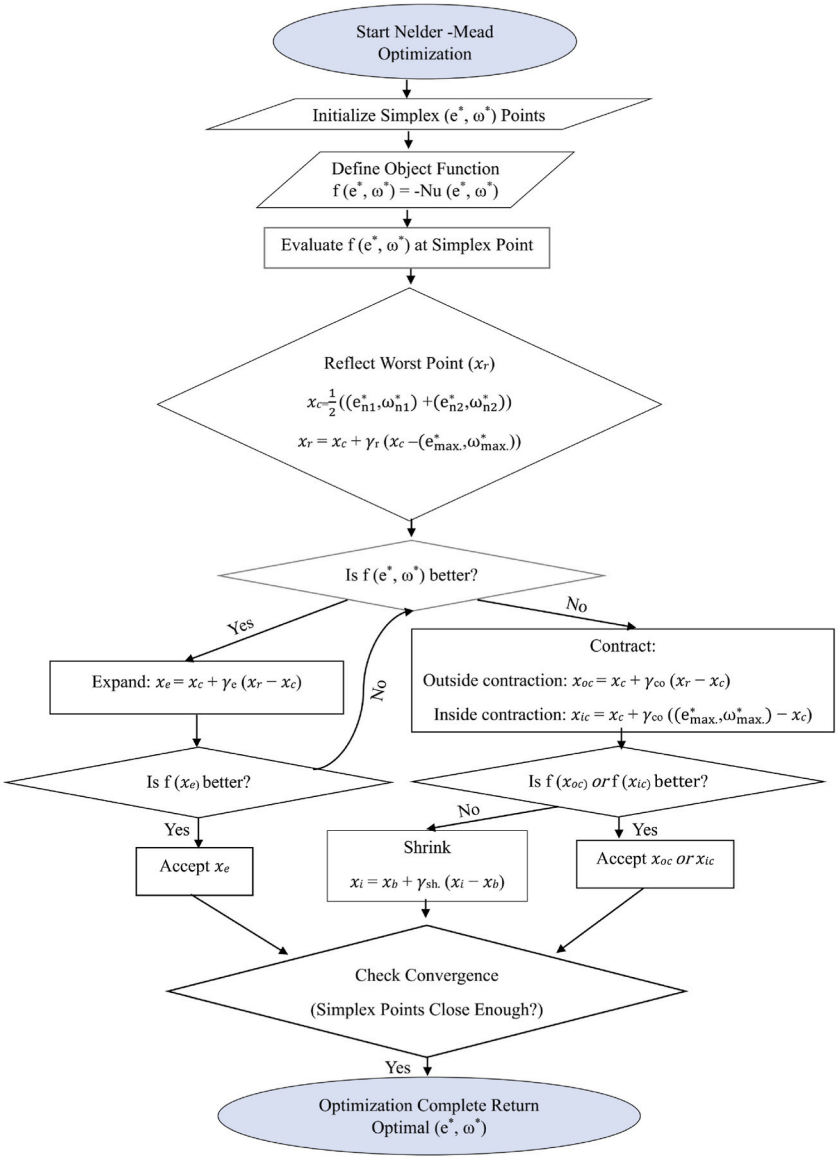

Fig. 3. Outline of optimization procedure.

making it worthwhile in cases where the function is not smooth or contains impurities or noise. The method is based on improving the search using a set of points that form a geometric structure, where these points interact according to the values of the function in an attempt to reach the optimal point [56].

The flowchart in Fig. 3 illustrates the steps of the optimization procedure, which include defining the configuration, applying the boundary conditions, identifying the representative variables e^* and ω^*, calculating the objective function $Nu(e^*, \omega^*)$, and determining the optimal value. The Nelder–Mead method was integrated with the numerical simulation, so that Nelder–Mead controlled the values of the parameters e^* and ω^*, and the numerical simulation returned the Nusselt number at $t^* = 0.15$. An initial guess of $e^* = 0.35$ and $\omega^* = 100$ was adopted to construct the initial simplex. The optimization was performed within the bounds e^* in (0.1, 0.4) and ω^* in (100, 400), with a stopping tolerance of 0.001 and a maximum of 40 iterations.

3.2. Verification of grid refinement

To evaluate convergence in a vessel containing cylinders, each with a radius of ($r^* = 0.05$), the Nusselt number, streamlines, and isotherms are examined. These cylinders are positioned at a distance of ($e^* = 0.35$) from the vessel's center and are subjected to angular velocities ranging from $\omega^* = 10$ to 400, with a Rayleigh number of (10^5) and a Prandtl number of (Pr = 6.9). The ratio of thermal conductivity (R_{th}) between the frame and the fluid and the ratio of heat capacity (R_h) is maintained constant at 397.63 and 0.582,

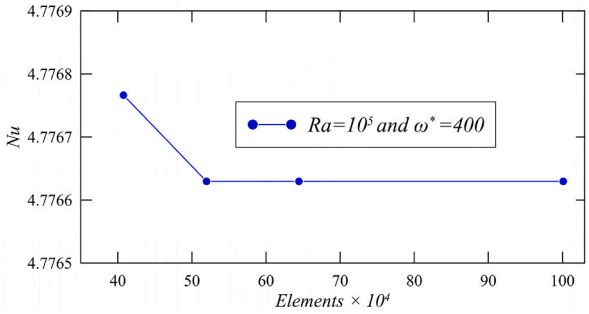

Fig. 4 (a). Assessment of grid dependency at $r^* = 0.05$, $t^* = 0.15$, $e^* = 0.35$, $Ra = 10^5$, and $\omega^* = 400$.

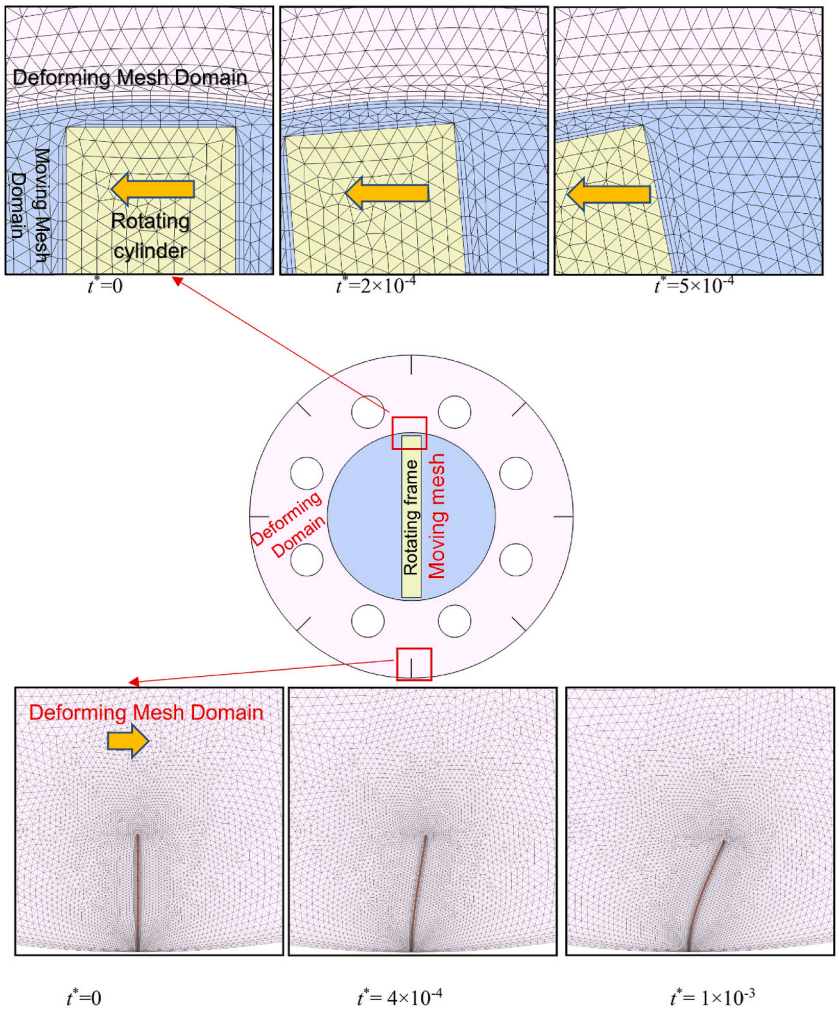

Fig. 4 (b). Visualization of the finalized mesh size, comprising 519,730 elements at rotating frame with different values of time by movement mesh at $\omega^* = 400$, $e^* = 0.35$ and $Ra = 10^5$.

respectively. The inner surface of the vessel is equipped with eight flexible baffles, characterized by Young's modulus of $E^* = 2\times 10^{10}$ and a thermal conductivity ratio between flexible baffles and fluid ($k_r = 13$). Various mesh sizes were evaluated, as depicted in Fig. 4 (a), with an optimal mesh size of 519,730 elements (illustrated in Fig. 4 (b)) selected to balance accuracy and computational efficiency. The figure illustrates the movement of the mesh within the rotating domain, where the mesh adapts to moving as the rotating frame moves while the other domain undergoes deformation. Three-time values were considered for this analysis.

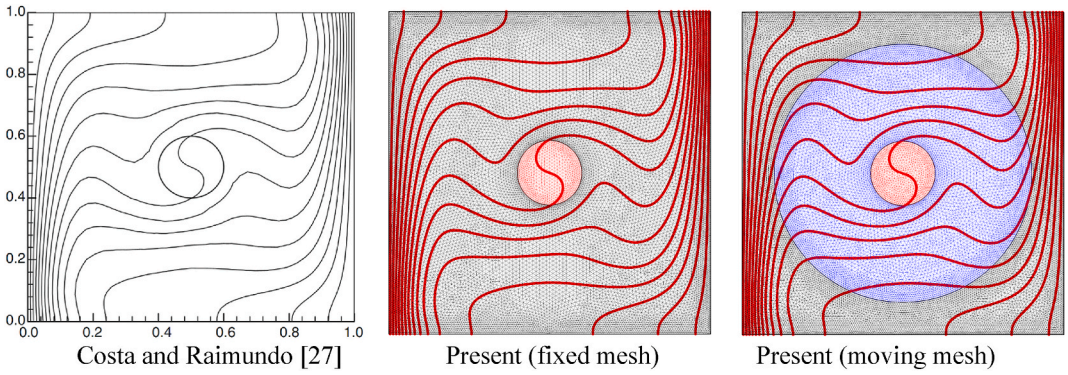

Fig. 5. Comparison with rotating circular cylinder [27] at Ra = 10^5, Pr = 0.7, ω* = 1000.

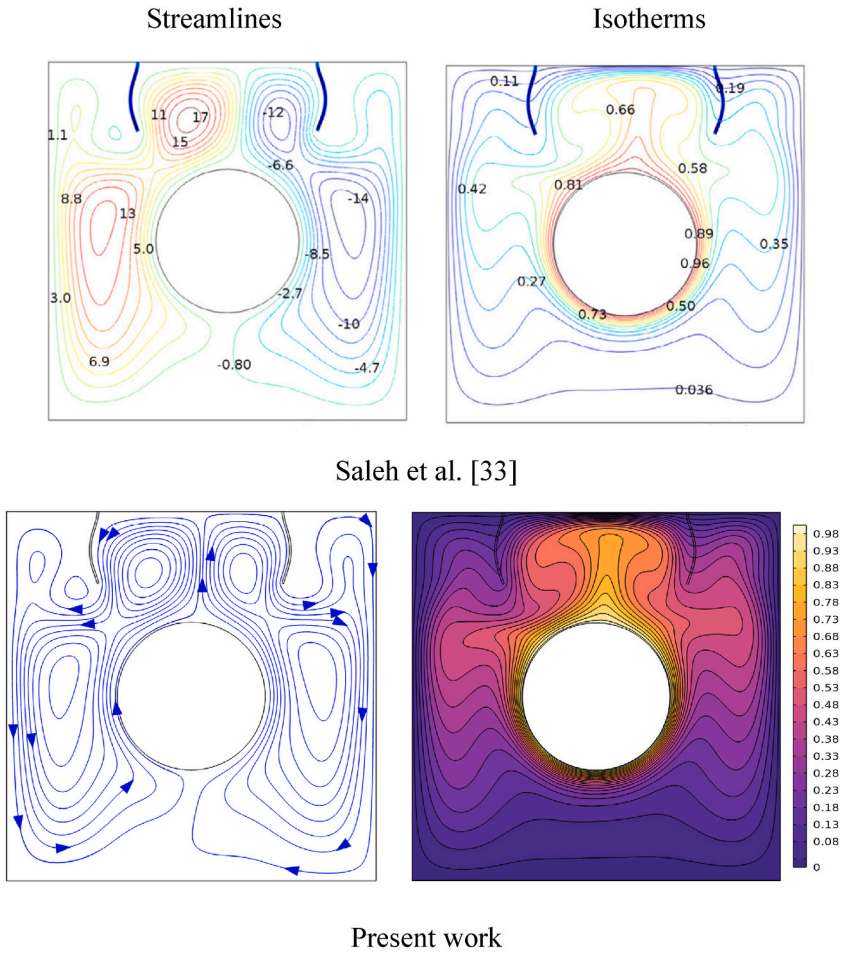

Fig. 6. Comparison with Saleh et al. [33], at the length of the fin (a^* = 0.2), elastic modulus (E^* = 10^9), oscillation amplitude (A^* = 0.1), radius of cylinder (R^* = 0.2), Ra = 10^6 and oscillation period ($t_p{}^*$ = 0.5) with t^* = 1.125 (4 $t_p{}^*$/8).

3.3. Verifications of results

The use of rotating meshes is a common technique in computational fluid dynamics to handle problems involving rotating components. For the sake of validation, a comparison was made with previously published numerical outcomes obtained by Costa and Raimundo [27] regarding the problem of mixed convection heat transfer in a cavity heated horizontally in the presence of a rotating cylinder. The isotherms were analyzed to focus on the utilization of fixed and rotating meshes, and to evaluate whether the rotating

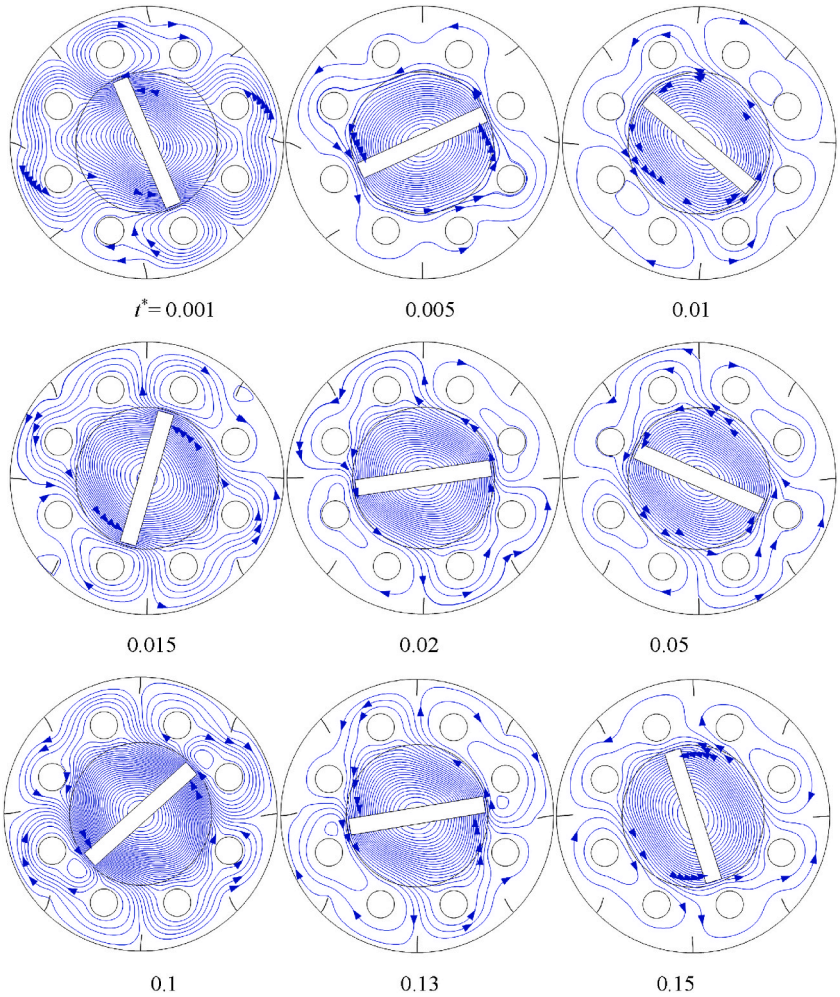

Fig. 7. Streamline contour progression for various intervals at $Ra = 10^5$, $r^* = 0.05$, $\omega^* = 400$, and $e^* = 0.35$.

mesh provides accurate details. Fig. 5 demonstrates what we hope namely, very good accurate details of the temperature distribution can be obtained using the rotating mesh.

To ensure the accuracy of the numerical method and achieve optimal results, a validation test was performed based on the work of Saleh et al. [33]. This test involved analyzing unsteady mixed convection in a square enclosure with a heated circular cylinder, complemented by two solid elastic thin fins attached to the top cold wall, each length (L). The governing parameters considered included the direction, amplitude, and length of fin oscillation, varying elasticity values, and cylinder sizes. The Prandtl number was kept constant at 0.7 (for air), while the Rayleigh number was fixed at 10^6. The cylinder was characterized by a radius (R). The comparison yielded excellent results, as demonstrated by the visualization of isotherms and streamlined contours shown in Fig. 6.

4. Results and discussion

The current study establishes the following dimensionless quantities to define the parameters: Water is the working fluid, with several Prandtl at (Pr = 6.9). The Rayleigh number is varied within the range of $10^3 \leq Ra \leq 10^5$, whereas the rotational frame as $10 \leq \omega^* \leq 400$, and the position of the cylinders varies as $0.32 \leq e^* \leq 0.43$. The thermal conductivity ratio between the frame and the fluid is denoted as (R_{th}), and the heat capacity ratio, (R_h), are held constant at 397.63 and 0.582, respectively.

In this investigation, four cold and four hot cylinders are distributed as shown in Fig. 1. Flexible baffles, with a Young's modulus of $E^* = 2 \times 10^{10}$, are attached to the inner surface of the vessel. The length of each baffle is denoted as $a_{fl.}$, and its width as $b_{fl.}$, with baffles evenly distributed between every two adjacent cylinders. We considered flexible baffles because Al-Hasan et al. [36] previously proved that they offer better performance than rigid baffles. At $\omega^* = 100$, flexible baffles show an 18 % advantage in Nusselt number and a 92 % advantage in overall performance. Therefore, this study focuses on developing optimum conditions using flexible baffles.

It is particularly interesting to examine the cyclic patterns of streamlines and isotherms and the time required to reach a steady state. The following subsection is dedicated to exploring this behavior.

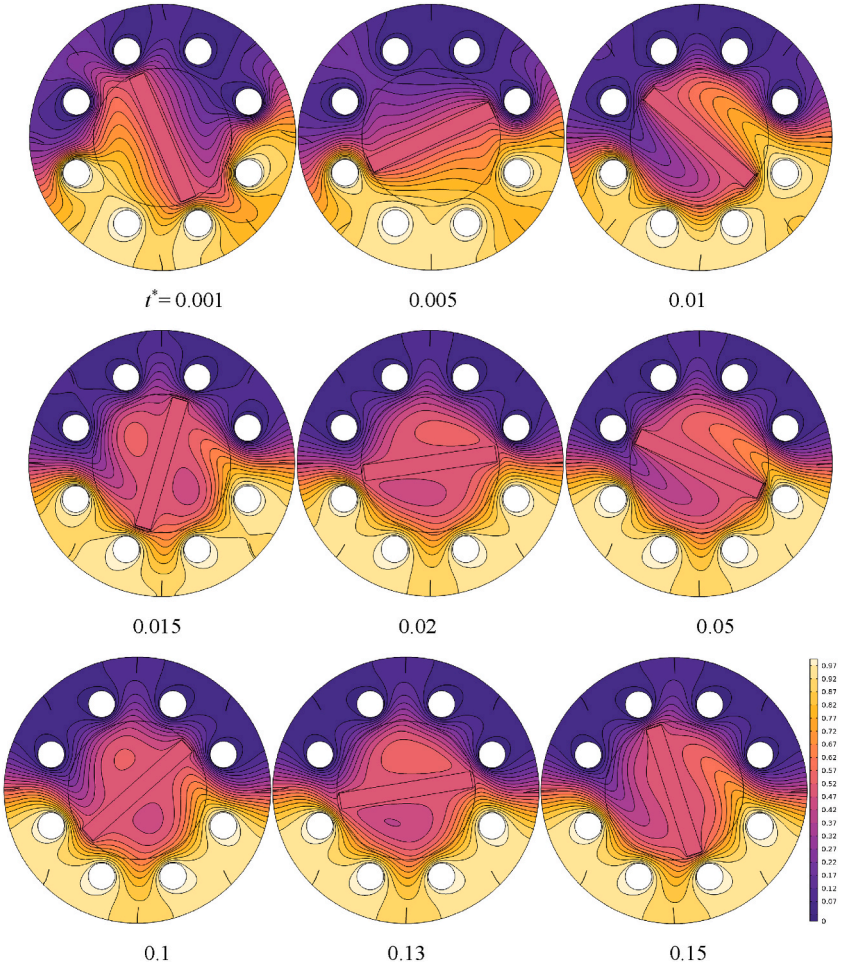

Fig. 8. Isotherms progression for various intervals at $Ra = 10^5$, $r^* = 0.05$, $\omega^* = 400$ and $e^* = 0.35$.

4.1. Transient results

The diagrams in Figs. 7 and 8 illustrate the streamlines and isotherms, highlighting the transient behaviors. Each cylinder has a fixed radius of ($r^* = 0.05$), and its centers are located at a distance of ($e^* = 0.35$) from the vessel's middle. The Rayleigh number is set at 10^5, and the rotating frame is 400. A time step of 0.001 is employed to achieve higher resolution, ensuring a more accurate representation of the frame's motion and the evolution of the streamlines.

At the start of the time simulation ($t^* = 0.001$), the heat flows are weak or almost non-existent, as the dynamic effect of the rotating frame and the flexible baffles have not yet started to move the thermal layers. The streamlined plots show straight or scattered lines around the hot and cold cylinders, with no significant overlap between the heat flows and no apparent movement in specific directions. At the intermediate time ($t^* = 0.05$) (before reaching stability), vortices form around the rotating frame, and the streamlined lines start to overlap. This implies to active interaction between the cold and hot cylinders. A clear differentiation between the heat flows appears as the streamlines move from the lower hot cylinders upwards towards the cold cylinders due to the free convection. The flexible baffles improve the heat distribution and redirect the flows towards the center. Here, the streamlines appear as circles or spirals around the rotating frame, increasing the complexity of the system's flows and enhancing the thermal motion. When the stability time is reached ($t^* = 0.13$), the system begins to reach thermal stability, where the flows become almost constant without significant changes, which expresses the state of thermal equilibrium. The streamlined drawings show regular and equal-length streamlines around the different regions, especially around the rotating frame. The streamlines become less overlapping, which reflects the balanced thermal distribution. This state indicates that both the cold and hot cylinders have distributed their heat homogeneously, and the flexible baffles no longer add significant oscillatory motions, which indicates to the fully equilibrium state.

Closer to the initial conditions, for the isotherms at $t^* = 0.001$, the heat is distributed unevenly inside the vessel, with high temperatures appearing in the hot lower cylinders while low temperatures occur in the cold upper cylinders. The isotherms appear far apart and do not overlap significantly, which expresses a clear temperature difference between the hot and cold regions. There is no significant effect of convection yet. In the intermediate time ($t^* = 0.05$), as the rotating frame begins to move and the thermal effect

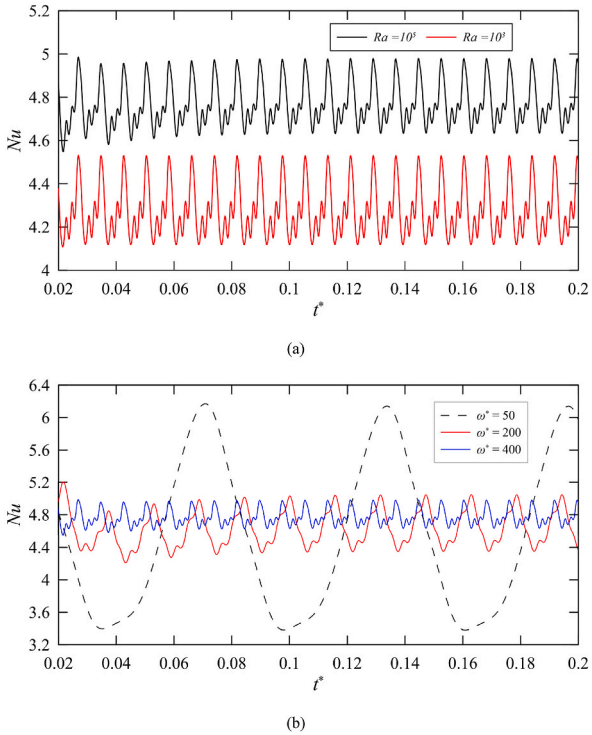

Fig. 9. Variation of the Nusselt number over time for $r^* = 0.05$ and $e^* = 0.35$: (a) at different *Ra* values with fixed $\omega^* = 400$, and (b) at different ω^* values with fixed $Ra = 10^5$.

resulting from the high Rayleigh number emerges, the isotherms bend and approach each other around the rotating frame. This improvement in heat distribution within the system is due to the frame's movement and the thermal interaction between the cylinders. A heat transfer zone is formed around the rotating frame, where the isotherms overlap and intensifies, indicating to increased heat exchange. The effect of the flexible baffles is evident in improving the heat distribution towards the periphery of the vessel, where the isotherm appears in a harmonious and flowing pattern that reflects the beginning of the formation of balanced heat flows. When the time of stability is reached ($t^* = 0.13$), the system reaches a thermal stability state, and the isotherm lines appear in a more uniform state as they are distributed evenly and symmetrically around the vessel. The equilibrium isotherm lines show that thermal equilibrium has been achieved, as there are no sharp temperature differences. The heat distribution is uniform due to vigorous convection effects and a high Rayleigh number, reflecting the final thermal equilibrium in the system, as shown in Fig. 8.

The Nusselt number shows a gradual increase with rising thermal activity, driven by variations in the Rayleigh number and a fixed high rotational frame of $\omega^* = 400$, as illustrated in Fig. 9(a). After $t^* = 0.13$, it reaches cyclic stability, signifying that the system has attained thermal equilibrium and consistent heat transfer performance. In Fig. 9(b), with the Rayleigh number fixed at 10^5 and varying rotational frame, the average Nusselt number also stabilizes beyond $t^* = 0.13$, confirming the steady-state nature of the heat exchange process.

4.2. Optimal design

This section presents and analyzes the results of calculations for determining the maximum design point of a system consisting of a vessel with hot cylinders at the bottom and cold cylinders at the top, with flexible baffles and a rotating frame in the middle. The main objective of this analysis is to study the effect of changing the Rayleigh number on the system (Ra = 10^3 and 10^5). Two main variables, rotational speed (ω^*) and distance cylinders to the frame axis (e^*), were adopted to determine the best design that achieves high thermal efficiency and system stability.

In Fig. 10, the streamlines are shown for different speeds and distances of the cylinders from the frame axis, where many values were taken to find the best values and find the best consistency for the flow lines at Rayleigh number = 10^5, the constant size of the cylinders at $r^* = 0.05$ and the time fixed at $t^* = 0.15$.

Regarding the streamlines, it was found that there is a clear pattern of consistency, especially near the rotating frame. This result confirms the effect of speed and distance between cylinders on improving flow distribution and reducing static areas. At certain speeds and with increasing Rayleigh numbers, the convection force in the system is enhanced, which leads to an improvement in the flow distribution around the cylinders. The flexible baffles significantly organize the flow lines when actuated by the moving frame. They direct the flow away from the heated cylinders while suppressing it near the cold cylinders, intensifying both the hot rising and cold

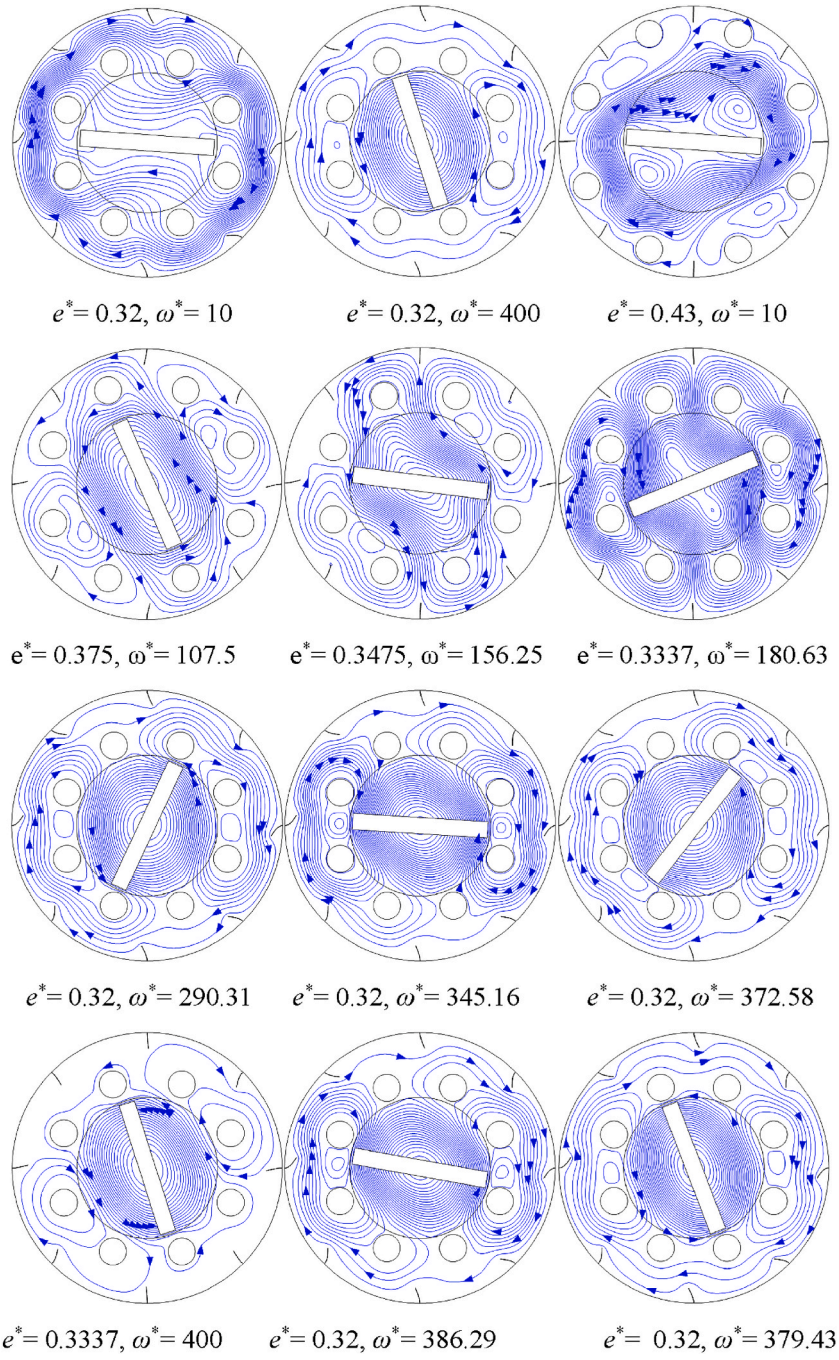

Fig. 10. Streamlines contours at $r^* = 0.05$, and $t^* = 0.15$ for variables e^* and ω^* at $Ra = 10^5$.

descending currents. This effect promotes effective interaction between the cooled and heated cylinders. The dynamic baffles adjust according to the rotating frame's motion, uniformly guiding the flow and reducing thermal hotspots by dispersing heat accumulation across the system. The uniformity of flow lines near the rotating frame promotes a balance of velocity and pressure distribution around the cylinders. This balance enhances the stability of heat flow and reduces the formation of high- or low-pressure areas. These results illustrate the importance of choosing the appropriate speeds of the rotor and the optimum distance between the cylinders to achieve a consistent distribution of flow lines, especially in systems that require efficient heat transfer. On the other hand, Fig. 11 shows the isotherms with variable $\omega^*$and e^* where the effect of different speeds and cylinder distances on the temperature distribution inside the vessel is visible. The symmetric isotherms are particularly noticeable at high Rayleigh number, where increased convection currents lead to a more efficient heat distribution within the medium.

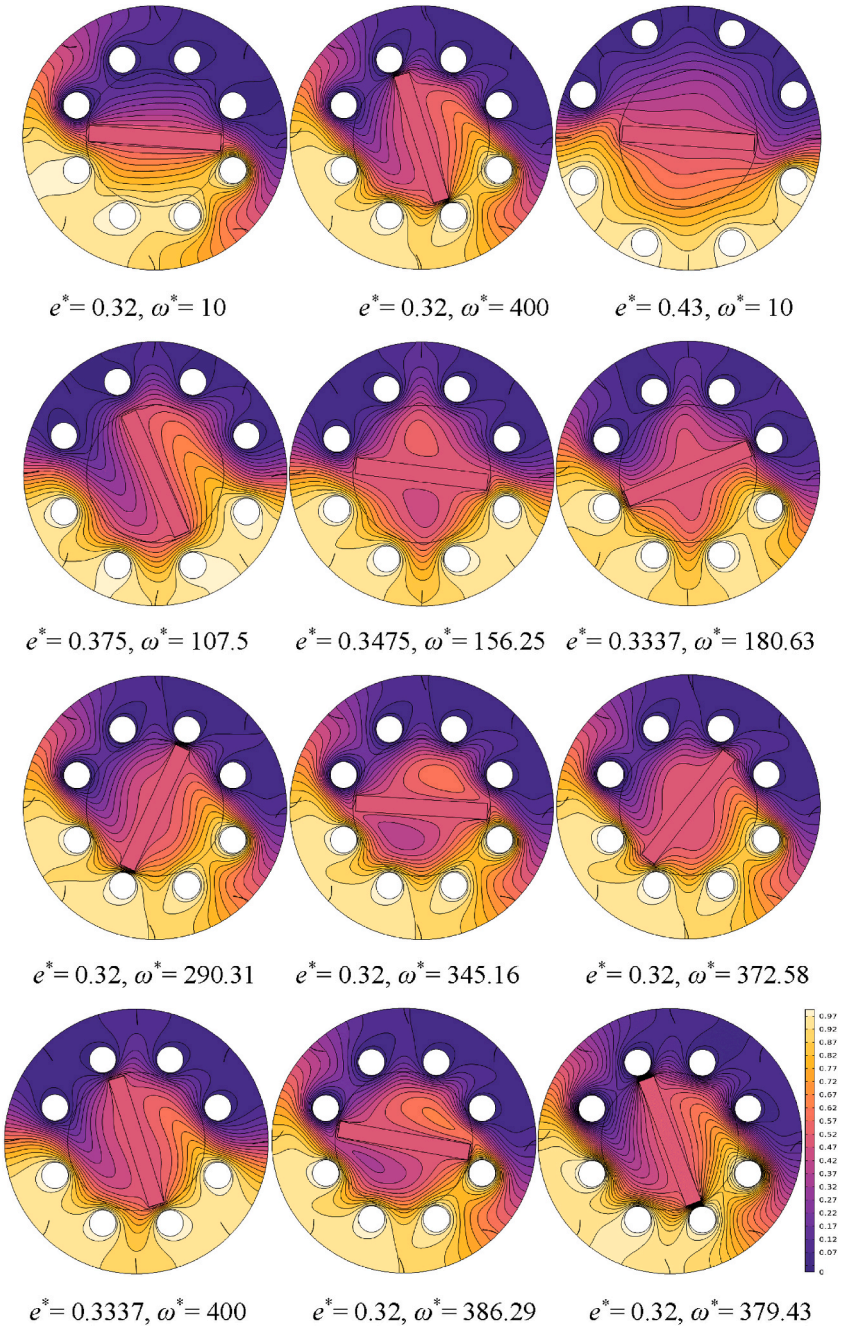

Fig. 11. Isotherms at $r^* = 0.05$, and $t^* = 0.15$ for variables e^* and ω^* at $Ra = 10^5$.

As the Rayleigh number increases, the isotherms become denser around the cylinders, indicating more rapid heat exchange. These lines are uniformly distributed within the hot and cold regions, maximizing heat exchange efficiency. This symmetry mitigates undesirable temperature drops and accelerates the system's thermal equilibrium. In this design, the flexible baffles bend with the rotating frame, promoting active bulk motion and a more uniform isotherms distribution throughout the system. They help in reducing the thermal differences between the different layers of fluids and reduce the formation of regions with constant temperatures (static areas), which allows direct heat toward the cylinders more efficiently. Thus, the baffles enhance heat transfer through the system.

Categorically, the Nusselt number (*Nu*) is presented with two main variables: the distance of the cylinders from the frame axis (e^*) and the speed of the rotating frame (ω^*). The first plot in Fig. 12 (a) shows the distribution of Nusselt number concerning these variables for Ra = 10^3. The analysis showed that the supreme point of Nusselt number under these conditions was achieved when the $e^* = 0.32378$ and $\omega^* = 366.48$, indicating that this dimension enhances heat exchange efficiency at that specific speed of the rotating

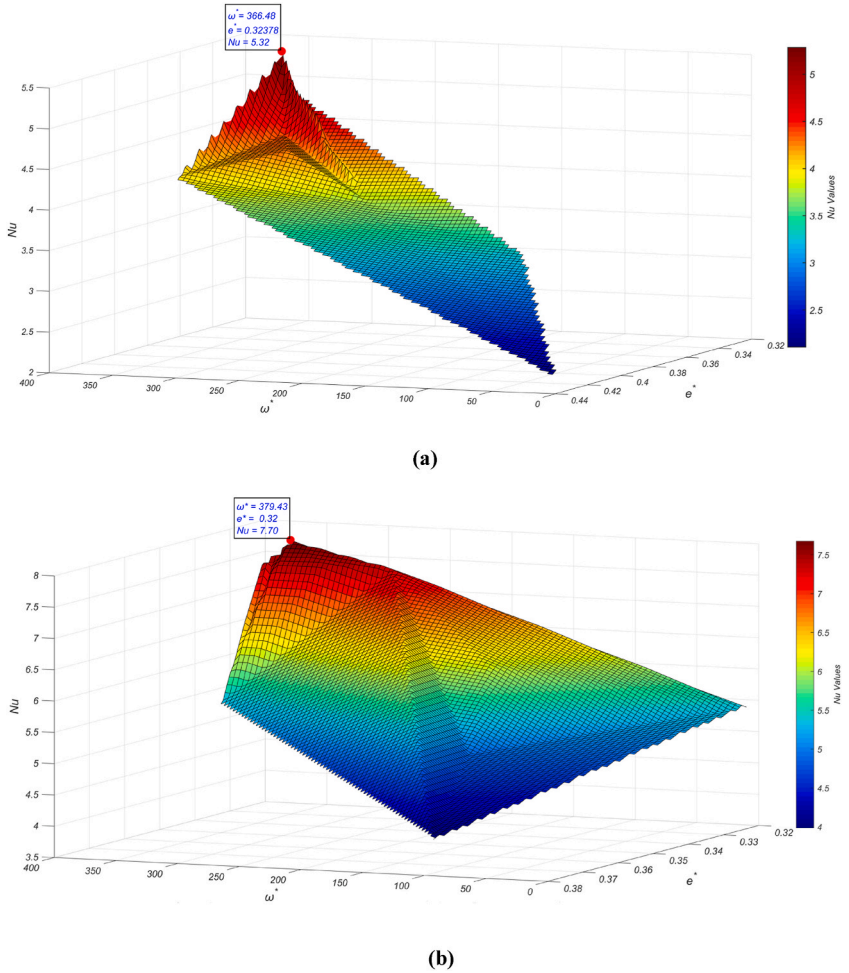

Fig. 12. Disrbuations of Nusselt number at $t^* = 0.15$ concerning rotational speed ω^* and e^*, considering $r^* = 0.05$ for **(a)** $Ra = 10^3$ and **(b)** $Ra = 10^5$.

frame. In the second plot in Fig. 12(b), the Nusselt number is calculated at a high value of Rayleigh number at $Ra = 10^5$, which represents the case of an intense thermal load. The results indicate that the maximum point of the Nusselt number can be reached at $e^* = 0.32$ and $\omega^* = 379.43$, which reflects the effect of thermodynamic factors more clearly under high thermal load conditions.

5. Conclusions

This study analyzes the design of a thermal vessel composed of cold upper cylinders and hot lower cylinders, enhanced by a rotating frame and flexible baffles to improve heat transfer efficiency. The performance was evaluated based on two primary variables: the speed of the rotating frame (ω^*) and the distance between the cylinders and the frame's axis (e^*) under Rayleigh conditions ($Ra = 10^3$ - 10^5). The main conclusions can be categorized as;

(i) At a low Rayleigh number (Ra = 10^3), optimal performance was achieved at a close distance from the center of rotation (e* = 0.32378), with a rotating frame speed of (ω* = 366.48). This provided the best balance between thermal current movement and heat transfer. Notably, although the maximum speed tested was 400, the speed of 366.48 demonstrated the highest system efficiency in terms of thermal balance, avoiding the need to reach maximum rotation speed.

(ii) At a high Rayleigh number (Ra = 10^5), the highest efficiency was obtained at a slightly closer proximity to the frame's axis (e* = 0.32), where the distance is somewhat reduced compared to the case of low Rayleigh number. The optimal speed in this scenario was ($\omega^* = 379.43$), close to the maximum tested speed of 400. This speed enhances thermal current movement under high thermal load conditions, maximizing the system's heat transfer efficiency.

(iii) Quantitatively, the optimum Nusselt numbers are 5.32 for Ra = 10^3 and 7.7 for Ra = 10^5.

6. Limitations and future research direction

This study is limited to Newtonian fluids and laminar flow. Optimization efforts were conducted for limited parameters (angular speed and cylinder positions) and two Rayleigh numbers. Future work can delve into the turbulent flow regime, and non-Newtonian fluids can be assessed. The optimization can be achieved with the aid of the Response Surface Methodology (RSM) technique.

CRediT authorship contribution statement

Ali Qassim Abd Al-Hassan: Writing – review & editing, Writing – original draft, Validation, Data curation, Conceptualization. **Muneer A. Ismael:** Writing – review & editing, Writing – original draft, Validation, Supervision, Resources, Methodology. **Mohammad Ghalambaz:** Writing – review & editing, Writing – original draft, Resources, Formal analysis. **Ali Chamkha:** Writing – review & editing, Supervision, Resources, Methodology. **Mohamed Bechir Ben Hamida:** Writing – review & editing, Writing – original draft, Validation, Software, Resources, Methodology, Funding acquisition.

Funding statement

This work was supported and funded by the Deanship of Scientific Research at Imam Mohammad Ibn Saud Islamic University (IMSIU) (grant number IMSIU-DDRSP-RP26).

Declaration of competing interest

The authors declare that they have no known competing financial interests or personal relationships that could have appeared to influence the work reported in this paper.

Data availability

Data will be made available on request.

References

[1] K. Thulukkanam, Heat Exchanger Design Handbook, CRC press, 2000 Feb 23.
[2] F. Incropera, D. DeWitt, Fundamentals of Heat and Mass Transfer, sixth ed., J. Wiley & Sons, New York, 2007.
[3] J.D. Deaton, R.V. Grandhi, A survey of structural and multidisciplinary continuum topology optimization: post 2000, Struct. Multidiscip. Optim. 49 (2014) 1–38.
[4] G.P. Steven, Q. Li, Y.M. Xie, Evolutionary topology and shape design for general physical field problems, Comput. Mech. 26 (2000) 129–139.
[5] N. Wiker, A. Klarbing, T. Borrvall, Topology optimization of regions of Darcy and Stokes flow, Int. J. Numer. Methods Eng. 69 (7) (2007) 1374–1404.
[6] Y. Deng, Z. Liu, Y. Wu, Topology optimization of steady and unsteady incompressible Navier-Stokes flows driven by body forces, Struct. Multidiscip. Optim. 47 (4) (2013) 555–570.
[7] S. Kreissl, K. Maute, Level set based fluid topology optimization using the extended finite element method, Struct. Multidiscip. Optim. 46 (2012) 311–326.
[8] S. Nørgaard, O. Sigmund, B. Lazarov, Topology optimization of unsteady flow problems using the lattice Boltzmann method, J. Comput. Phys. 307 (2016) 291–307.
[9] A.A. Koga, E.C.C. Lopes, H.F. Villa Nova, C.R. Lima, E.C.N. Silva, Development of heat sink device by using topology optimization, Int. J. Heat Mass Tran. 64 (2013) 759–772.
[10] J. Alexandersen, N. Aage, C.S. Andreasen, O. Sigmund, Topology optimization for natural convection problems, Int. J. Numer. Methods Fluid. 76 (10) (2014) 699–721.
[11] P. Coffin, K. Maute, A level-set method for steady-state and transient natural convection problems, Struct. Multidiscip. Optim. 53 (5) (2016) 1047–1067.
[12] R. Picelli, W.M. Vicente, R. Pavanello, Evolutionary topology optimization for structural compliance minimization considering design-dependent FSI loads, Finite Elem. Anal. Des. 135 (2017) 44–55.
[13] A. Bangian-Tabrizi, Y. Jaluria, An optimization strategy for the inverse solution of a convection heat transfer problem, Int. J. Heat Mass Tran. 124 (2018) 1147–1155.
[14] V. Subramaniam, T. Dbouk, J.-L. Harion, Topology optimization of conjugate heat transfer systems: a competition between heat transfer enhancement and pressure drop reduction, Int. J. Heat Fluid Flow 75 (2019) 165–184.
[15] B. Kwon, L. Liebenberg, A.M. Jacobi, W.P. King, Heat transfer enhancement of internal laminar flows using additively manufactured static mixers, Int. J. Heat Mass Tran. 137 (2019) 292–300.
[16] J. Chen, B. Xia, C. Zhao, Topology optimization for heat transfer enhancement in thermochemical heat storage, Int. J. Heat Mass Tran. 154 (2020) 119785.
[17] T. Dehghani, F.S. Moghanlou, M. Vajdi, M.S. Asl, M. Shokouhimehr, M. Mohammadi, Mixing enhancement through a micromixer using topology optimization, Chem. Eng. Res. Des. 161 (2020) 187–196.
[18] K. Li, J. Wen, S. Wang, Y. Li, Multi-parameter optimization of serrated fins in plate-fin heat exchanger based on fluid-structure interaction, Appl. Therm. Eng. 176 (2020) 115357.
[19] C.-Y. Wu, Numerical modeling of hydrogen catalytic reactions over a circular bluff body, Int. J. Hydrogen Energy 47 (2022) 37204–37217.
[20] H. Li, T. Qi, Y. Zhang, Effect of furnace structure on burden distribution and gas flow in sinter vertical cooling furnace, Appl. Sci. 13 (2023) 11268.
[21] X.-X. Chen, R.-B. Chen, C.-Y. Wu, Prediction and optimization of heat transfer performance of premixed methane impinging flame jet using the kriging model and genetic Algorithm, Appl. Sci. 14 (2024) 3731.
[22] J. Alexandersen, C.S. Andreasen, A review of topology optimization for fluid-based problems, Fluids 5 (2020) 29.
[23] F. Lucchini, R. Torchio, V. Cirimele, P. Alotto, P. Bettini, Topology optimization for electromagnetics: a survey, IEEE Access 10 (2022) 98593–98611.
[24] T.W. Rees, A. Azam, N. Casari, P. Banks, L. Jiranek, S. Furino, A. Muley, An experimental case Study in combining topology optimization and additive manufacturing techniques to generate novel and high-performance compact heat exchanger designs, in: Turbo Expo: Power for Land, Sea, and Air, American Society of Mechanical Engineers, 2024. V013T013A040.
[25] K. Gangadhar, M.R. Lavanya, A. Wakif, Impact of wall slip and jump in the heat transmission enhancement of copper-alumina/water hybrid nanofluid due to a stretched cylinder, Int. J. Ambient Energy 45 (2024).

[26] A.Q. Abd Al-Hasan, M.A. Ismael, M. Ghalambaz, Heat transfer in a vessel-tubes array with a rotating baffle: a rotating frame modeling approach, Int. J. Thermofluids 22 (2024) 100659.
[27] V.A.F. Costa, A.M. Raimundo, Steady mixed convection in a differentially heated square enclosure with an active rotating circular cylinder, Int. J. Heat Mass Tran. 53 (5–6) (2010) 1208–1219.
[28] A.M. Hassan, M.A. Alomari, Q.H. Al-Salami, F. Alqurashi, M.A. Flayyih, A.M. Sadeq, Numerical analysis of MHD combined convection for enhanced CPU cooling in NEPCM-filled a trapezoidal cavity, Int. Commun. Heat Mass Tran. 159 (2024 Dec 1) 108343.
[29] A.M. Hassan, M.A. Alomari, Q.H. Al-Salami, F.Q. Alyousuf, F. Alqurashi, M.A. Flayyih, Active cooling of hot integrated circuits using a rotating cylinder and NEPCM-water mixture: numerical analysis of the impact of phase change and Magnetohydrodynamics on double-diffusive mixed convection, Int. Commun. Heat Mass Tran. 159 (2024 Dec 1) 107987.
[30] A.M. Hassan, M.A. Alomari, Q.H. Al-Salami, F.A. Alyousuf, F. Alqurashi, M.A. Flayyih, Numerical analysis of hydrothermal performance and entropy generation in an active cooling system: a case study with NEPCM, double-diffusive mixed-convection and MHD, Case Stud. Therm. Eng. 61 (2024 Sep 1) 105064.
[31] H.W. Ayoob, I. Omar, W.K. Ghanim, M.N. Fares, M.A. Fazilati, S. Salahshour, S. Esmaeili, The thermal-flow performance of water-Al_2O_3 nanofluid flow in an elliptical duct heat exchanger equipped with two rotating twisted tapes, Case Stud. Chem. Environ. Eng. 11 (2025 Jun 1) 101094.
[32] M. Al-Saad, A.B. Ali Ab, M. Al-Mosallam, M.N. Fares, M.A. Fazilati, S. Salahshour, R. Sabetvand, Ag and Al_2O_3/water two-phase transient flow analysis in a double-pipe heat exchanger equipped with baffles and rotating inner tube, Case Stud. Chem. Environ. Eng. (2025 Jan 27) 101117.
[33] H. Saleh, Z. Siri, I. Hashim, Role of fluid-structure interaction in mixed convection from a circular cylinder in a square enclosure with double flexible oscillating fins, Int. J. Mech. Sci. 161 (2019) 105080.
[34] M.B. Ben Hamida, Fluid-Structure interaction analysis in natural convection heat transfer inside a T-shaped cavity with a flexible baffle, J.Nanofluid 11 (2022) 169–191.
[35] M.B. Ben Hamida, Investigation of fluid-structure interaction and heat transfer dynamics in a wavy L-shaped enclosure with an elastic baffle, Int. Commun. Heat Mass Tran. 162 (2025) 108617.
[36] A.Q.A. Al-Hassan, M.A. Ismael, M. Ghalambaz, Modeling of rotating frame within a cylindrical vessel containing isothermal cylinders equipped with flexible radial baffles, ASME J. Heat Mass Transfer 147 (9) (2025) 092602.
[37] M.M. Ikram, G. Saha, S.C. Saha, Conjugate forced convection transient flow and heat transfer analysis in a hexagonal, partitioned, air-filled cavity with dynamic modulator, Int. J. Heat Mass Tran. 167 (2021) 120786.
[38] M.M. Ikram, G. Saha, S.C. Saha, Unsteady conjugate heat transfer characteristics in a hexagonal cavity equipped with a multi-blade dynamic modulator, Int. J. Heat Mass Tran. 200 (2023) 123527.
[39] M.M. Ikram, G. Saha, S.C. Saha, Second law analysis of a transient hexagonal cavity with a rotating modulator, Int. J. Heat Mass Tran. 221 (2024) 125039.
[40] B. Jalili, H. Roshani, P. Jalili, D.D. Ganji, Numerical study of Newtonian fluid flow characteristics in a triangular enclosure considering various obstacle geometries, Int. J. Thermofluids 20 (2023) 100515.
[41] B. Jalili, M. Emad, E.H. Malekshah, P. Jalili, A. Akgül, M.K. Hassani, Investigating double-diffusive natural convection in a sloped dual-layered homogeneous porous-fluid square cavity, Sci. Rep. 14 (2024) 7193.
[42] B. Jalili, M. Bahmani, P. Jalili, D. Liu, A.A. Alderremy, D.D. Ganji, M. Vivas-Cortez, Investigating the influence of square size vanes on heat transfer in porous media: an in-depth Nusselt distribution, J.Computational Des. Eng. 12 (2025) 1–4.
[43] H. Roshani, P. Jalili, B. Jalili, I. Ahmad, A.S. Hendy, M.R. Ali, D.D. Ganji, The effect of magnetic field on heat transfer in a porous medium octagonal cavity with Cassini oval barriers, Case Stud. Therm. Eng. 56 (2024) 104194.
[44] M. Bahmani, M. Babagoli, P. Jalili, B. Jalili, D.D. Ganji, Numerical study of a porous cavity with different square size vanes with a high focus on the Nusselt number, Int. J. Thermofluids 24 (2024) 100860.
[45] P. Zhang, H. Roshani, P. Jalili, B. Jalili, H. Alotaibi, D.D. Ganji, Thermal analysis of transient MHD ferrofluid flow and natural convection in a porous cavity with a cylindrical barrier, Case Stud. Therm. Eng. 66 (2025) 105693.
[46] K. Wu, F. Huang, J. Shen, A new class of higher-order decoupled schemes for the incompressible Navier-Stokes equations and applications to rotating dynamics, J. Comput. Phys. 458 (2022) 111097.
[47] S.H. Menon, J. Mathew, J. Jayaprakash, Derivation of navier–stokes equation in rotational frame for engineering flow analysis, Int. J. Thermofluids 11 (2021) 100096.
[48] F. Ali, S. Murtaza, N.A. Sheikh, I. Khan, Heat transfer analysis of generalized Jeffery nanofluid in a rotating frame: Atangana–Balaenu and Caputo–Fabrizio fractional models, Chaos Solitons Fractals 129 (2019) 1–15.
[49] J. Bonet, R.D. Wood, Nonlinear Continuum Mechanics for Finite Element Analysis, Cambridge University Press, 1997.
[50] Y.-C. Shih, J. Khodadadi, K.-H. Weng, A. Ahmed, Periodic Fluid Flow and Heat Transfer in a Square Cavity due to an Insulated or Isothermal Rotating Cylinder, 2009.
[51] O. Schenk, K. Gärtner, Solving unsymmetric sparse systems of linear equations with PARADISO, Future Gener. Comput. Syst. 20 (3) (2004) 475–487.
[52] P. Wriggers, Nonlinear Finite Element Methods, Springer Science & Business Media, 2008.
[53] F. Verbosio, A. De Coninck, D. Kourounis, O. Schenk, Enhancing the scalability of selected inversion factorization algorithms in genomic prediction, J. Comput. Sci. 22 (2017) 99–108.
[54] M. Bollhofer, A. Eftekhari, S. Scheidegger, O. Schenk, Large-scale sparse inverse covariance matrix estimation, SIAM J. Sci. Comput. 41 (2019) A380–A401.
[55] M. Bollhöfer, O. Schenk, R. Janalik, S. Hamm, K. Gullapalli, State-of-the-art sparse direct solvers. Parallel Algorithms in Computational Science and Engineering, 2020, pp. 3–33.
[56] B.K. Dora, S. Bhat, S. Halder, I. Srivastava, Multi-objective optimal power flow problem using Nelder–Mead based Prairie Dog optimization algorithm, Soft Comput. (2024) 1–34.